Materials Today Bio 29 (2024) 101355

Contents lists available at ScienceDirect

Materials Today Bio

journal homepage: www.journals.elsevier.com/materials-today-bio

Nanoplatform for synergistic therapy constructed via the co-assembly of a reduction-responsive cholesterol-based block copolymer and a photothermal amphiphile

Yue Lu [a], Tiantian Cai [a], Juanjuan Gao [a], Yangge Ren [a], Yi Ding [a], Shujing Liu [a], Linyuan Liu [a], Hao Huang [a], Haijie Wang [b], Chengji Wang [b], Wei Wang [c,****], Ruling Shen [b,***], Bo Zhu [a,**], Lin Jia [a,*]

[a] Department of Polymer Materials, School of Materials Science and Engineering, Shanghai University, Nanchen Street 333, Shanghai, 200444, China
[b] Shanghai Laboratory Animal Research Center, Jinke Street 3577, Shanghai, 201203, China
[c] Geriatric Medicine Department, The Fifth Affiliated Hospital of Southern Medical University, Congcheng Street 566, Guangzhou, 510920, China

A B S T R A C T

The goal of combination cancer therapy, including chemo-phototherapy, is to achieve highly efficient antitumor effects while minimizing the adverse reactions associated with conventional chemotherapy. Nevertheless, enhancing the contribution of non-chemotherapeutic strategies in combination therapy is often challenging because this requires multiple active ingredients to be encapsulated in a single delivery system. However, most commonly used photothermal reagents are challenging to be loaded in large quantities and have poor biocompatibility. Herein, we developed photothermal co-micelles through a co-assembly strategy using a cholesterol-based liquid crystal block copolymer (LC-BCP) with disulfide bonds in the side chain of the LC blocks and a croconaine-based amphiphile (CBA) containing a cholesterol moiety. This approach allowed the CBA to be effectively embedded within LC-BCPs, serving as the functional component of the drug-loaded carrier. These co-micelles could encapsulate doxorubicin (DOX), showed tunable reduction-responsive drug release, and enabled near-infrared laser-triggered photothermal therapy as well as *in vivo* fluorescence and photothermal imaging. Following laser irradiation, the photothermal activity of the co-micelles rapidly induced tumor cell death and accelerated drug release. *In vitro* and *in vivo* experiments demonstrated that the synergistic photo-chemotherapeutic effects of these drug-loaded co-micelles offer a promising avenue for synergistic precision photothermal-chemotherapy.

1. Introduction

The treatment of malignant tumors remains a major challenge, and intensive research is required to achieve advancements in this area. Currently, chemotherapy is a standard approach for cancer treatment [1]. However, despite improvements in outcomes due to the development of effective chemotherapeutic drugs, systemic chemotherapy is still associated with serious adverse effects [2–4]. Thus, it is essential to develop optimized treatment strategies that balance therapeutic efficacy with the prevention of chemotherapy-induced toxicity. In order to achieve this goal, there has been increased focus on attaining precise and controlled drug release. Additionally, combinations of chemotherapy with other treatments are actively being explored to minimize antitumor drug doses while improving treatment efficacy [5–8].

Photothermal therapy (PTT) via near-infrared (NIR) light irradiation has emerged as a valuable tool for synergistic treatment in combination with chemotherapy due to its distinct non-invasive nature, superior tissue penetration ability, tissue-specific characteristics, and heat-induced tumor ablation activity [9–15]. Among various photothermal agents, organic NIR-responsive dyes such as indocyanine green [16,17], phthalocyanine [18], porphyrins [19], and croconaine-based NIR dyes [20] are increasingly favored for their excellent photothermal conversion properties and flexible chemical structures. These agents also facilitate NIR bioimaging and are thus powerful candidates for imaging-guided phototherapy [21]. Moreover, encapsulating NIR-responsive dyes with antitumor drugs in stimuli-responsive carriers—such as pH [22], glutathione (GSH) [23,24], and enzyme-responsive [25,26] synthetic polymers or

* Corresponding author.
** Corresponding author.
*** Corresponding author.
**** Corresponding author.
E-mail addresses: ww7411@126.com (W. Wang), shenruling@slarc.org.cn (R. Shen), bozhu@shu.edu.cn (B. Zhu), jlsioc@shu.edu.cn (L. Jia).

https://doi.org/10.1016/j.mtbio.2024.101355
Received 29 July 2024; Received in revised form 4 November 2024; Accepted 20 November 2024
Available online 21 November 2024

biomacromolecules—allows for the creation of chemo-photothermal therapeutic systems. Upon exposure to NIR light, the photothermal effect accelerates drug release and simultaneously induces hyperthermia, leading to efficient tumoricidal effects via synergistic therapy [27–33].

However, the significant structural differences between carrier materials and conjugated NIR dyes typically lead to poor compatibility and low encapsulation efficiency [34]. In such treatment models, chemotherapy remains the primary mode of treatment, with phototherapy serving as a supplementary approach [35,36]. Although this synergistic combination achieves more efficient therapeutic effects than chemotherapy alone, the risk of toxic side effects persists. Many commonly used NIR-responsive molecules are as toxic as certain chemotherapeutic agents [37], and lack therapeutic effects after irradiation, raising concerns about their potential release from carrier platforms post-irradiation, which could induce additional side effects [38,39]. These challenges — namely, poor compatibility, high toxicity of NIR molecules, low stability of polymer carriers, and premature release of active ingredients — must be addressed to minimize toxic effects and achieve good therapeutic outcomes through the synergetic action of PTT and controlled drug release.

In this study (see Scheme 1), we synthesized a series of cholesterol-based liquid crystal block copolymers (LC-BCPs), which have attracted considerable interest in drug carrier design due to their inherent biocompatibility and non-toxic nature [40]. Considering the significance of redox reactions in biological systems, particularly due to differential concentrations of glutathione (GSH) between intracellular and extracellular environments [41], we introduced disulfide (SS) bonds into the side chains of the LC blocks of BCPs. This enabled the LC-BCPs to undergo reduction-triggered cleavage via exchange reactions with GSH [42,43]. The micelles formed by these LC-BCPs exhibited remarkable stability owing to their LC ordered arrangement. The reduction-responsive behavior of these micelles was tunable because it was dependent on the disulfide bond content and LC ordering effect. Additionally, we also designed and synthesized a croconaine-based amphiphile (CBA) for combined therapy following NIR laser irradiation. This novel structure — which included a polyethylene glycol (PEG) and cholesterol moiety on both sides of the croconaine center — ensured water solubility and facilitated the formation of co-micelles with BCPs through a synergistic co-assembly process [44], instead of simple encapsulation. This co-assembly method effectively increased the proportion of the photothermal agents in the final drug-loaded polymeric carriers containing doxorubicin (DOX), leading to the induction of tumor cell death primarily via laser irradiation. Meanwhile, the photothermal behavior of the co-micelles accelerated the release of the loaded DOX molecules, bridging the treatment gap post-irradiation. Both *in vitro* and *in vivo* experiments demonstrated the synergistic photothermal-chemotherapeutic effects of the drug-loaded co-micelles. This study provides valuable insights into the development of combined anticancer therapies. Additionally, it introduces a novel approach for fabricating multifunctional drug carriers to mitigate the risk of adverse effects associated with antitumor drugs, thereby meeting clinical requirements.

2. Materials and methods

2.1. Materials

Cholesteryl chloroformate (>98 %), 4-dimethylaminopyridine (DMAP, >99 %), 1-(3-dimethylaminopropyl)-3-ethylcarbodiimide hydrochloride (EDC, >98 %), trimethylamine (TEA, >99 %), 2-hydroxyethyl disulfide (>98 %), acryloyl chloride (>98 %), and croconic acid (CroA) were purchased from TCI and used as received. Dichloromethane (DCM) was distilled over CaH_2 and tetrahydrofuran (THF), dioxane were distilled over sodium shavings. Oligoethylene glycol methacrylate (OEGMA, $M_n = 300$) were purchased from Sigma-Aldrich and was filtered through a short column of neutral Al_2O_3 to remove the inhibitor before use. 2,2′-azobis(2-methylpropionitrile) (AIBN) was obtained from Acrose chemicals and recrystallized from ethanol. Anhydrous methanol (MeOH), ethyl acetate, acetic acid, diethyl ether, magnesium sulfate anhydrous ($MgSO_4$), tosyl chloride (TsCl), 1,6-hexanediol were purchased from Sinopharm Chemical Reagent Co., Ltd. Doxorubicin hydrochloride (DOX·HCl, 98 %) and glutathione (GSH, 95 %) were supplied by Aladdin. Dulbecco's modified Eagle medium (DMEM), fetal bovine serum (FBS), penicillin-streptomycin solution,

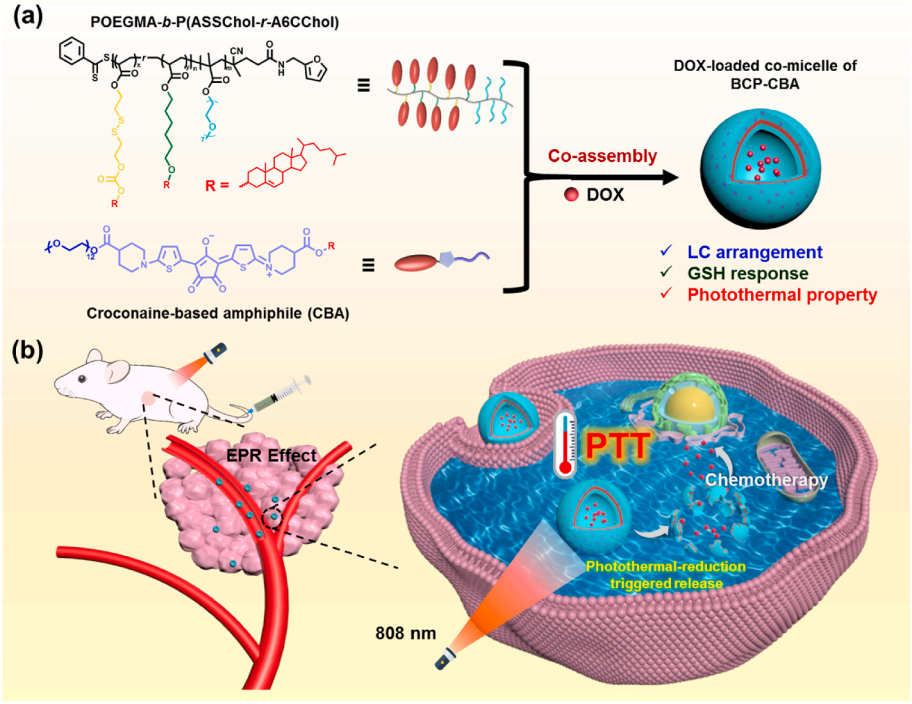

Scheme 1. Schematic illustration of (a) the preparation of DOX-loaded co-micelles and (b) synergistic photothermal-chemotherapy.

trypsin, 4′,6-diamidino-2-phenylindole (DAPI), Calcein-AM/PI Double Staining Kit, Cell Counting Kit-8 (CCK-8) were purchased from Titan. 1-(thiophen-2-yl)piperidine-4-carboxylic acid (SP-COOH) was synthesized by Ref. [45]. Furan-functionalized chain transfer agent (furan-CTA) was synthesized according to a literature reference [46].

2.2. Instrumentation

^{1}H NMR spectra were recorded on a Bruker AV 500 (500 MHz) spectrometer using $CDCl_3$ as the solvent. Chemical shifts were reported as values (ppm) relative to standard tetramethylsilane (TMS). Each spectrum was acquired with 64 scans and a relaxation delay of 10 s.

Gel permeation chromatography (GPC) was performed using three Waters Styragel columns (HR2/HR3/HR4) with THF as the mobile phase at a flow rate of 1 mL/min at 30 °C. Calibration was performed with polystyrene (PS) standards kit (Polymer Laboratory Co. Ltd., UK). Disulfide bond cleavage in block copolymers was analyzed by recording GPC before and after treatment with glutathione (GSH) as the reducing agent. Typically, 10 mg of copolymers was dissolved in 1 mL of THF, followed by the addition of 1.54 mg of GSH to achieve a final concentration of 10 mM. After stirring the solution for 6 h or 24 h, a 100 μL of the solution was directly injected to the GPC system for analysis.

Differential scanning calorimetry (DSC) analyses were carried out on a TA Q200 differential scanning calorimeter, calibrated using indium standards. Samples were initially scanned from −20 to 200 °C at a scanning rate of 10 °C/min. After reaching to 200 °C, the samples were held isothermally for 2 min and then cooled from 200 to −20 °C at the same rate. A second scan was conducted following the same procedure.

Liquid crystal textures were observed using a Motic BA310Met microscope in polarized optical microscope (POM) mode, equipped with an INSTEC HCS402 hot stage. The sample on the slide was first heated at 10 °C above the isotropic-to-liquid crystalline transition temperature ($T_{LC\text{-}I}$) determined by DSC analysis and maintained at this temperature for 30 min. Subsequently, the sample was cooled to 10 °C below the $T_{LC\text{-}I}$ and held at this temperature for 30 min.

Small angle X-ray scattering (SAXS) experiments were conducted on the BL16B1 beamline in the Shanghai Synchrotron Radiation Facility (SSRF). The wavelength of X-ray radiation was 1.24 Å and the sample-to-detector distance was 5 m. The exposure time for each measurement was 10 s. All experiments were performed at room temperature.

Bright-field transmission electron microscopy (TEM) images were obtained using a JEM-2100 instrument. A drop of solution was placed on a Formvar-carbon coated TEM grid, and after 15 min, excess liquid was wicked away by touching the droplet with the edge of a filter paper. The samples were then stained with 0.2 wt% uranyl acetate for 30 min, and the excess solution was removed with a filter paper.

UV/vis spectroscopy measurements were performed on a JASCO UV/vis spectrophotometer (V-550). The cuvette thickness was 10 mm, with a scanning rate of 400 nm/min and data interval was 0.5 nm. Fluorescence (FL) spectra were recorded using a Horiba Jobin Yvon Fluorolog-3 spectrophotometer.

2.3. Synthesis

The synthetic routes of two cholesterol-based acrylate monomers are shown in Schemes S1-2. The main difference between two monomers is the spacer linking the cholesterol and acrylate moieties. The monomer with a disulfide bond is denoted as ASSChol, whereas the monomer with hexanediol linker is denoted A6CChol. Details of the synthetic procedures are described in the Supporting Information. The chemical structures of the monomers were characterized by ^{1}H NMR (Figs. S1–2).

2.3.1. Synthesis of liquid crystalline block copolymers (LC-BCP)

POEGMA$_n$. POEGMA homopolymer was synthesized via reversible addition-fragmentation chain transfer (RAFT) using furan-CTA and oligoethylene glycol methacrylate (OEGMA, M_n = 300) as monomer (Scheme S3). Typically, furan-CTA (0.268 g, 0.75 mmol) and OEGMA (4.5 g, 15.0 mmol) were added into a 50 mL Schlenk flask under a nitrogen atmosphere. A solution of AIBN (0.025 g, 0.15 mmol) in dioxane (5 mL) was then added dropwise. The flask was degassed with three freeze-pump-thaw cycles and immersed in an oil bath at 60 °C. After 5 h of reaction, the solution was quenched by immersing the flask in liquid nitrogen. The resulting solution was concentrated under vacuum using a rotary evaporator, and the polymer was purified by three dissolution-sedimentation cycles in DCM (0.5 mL × 3) and diethyl ether (45 mL × 3). Finally, the polymer was dried under vacuum for 24 h (1.8 g, yield: 40 %). ^{1}H NMR (500 MHz, $CDCl_3$): δ (ppm) = 7.90 (d, 2H), 7.56 (t, 1H), 7.33–7.42 (m, 3H), 6.32 (t, 1H), 6.24 (d, 1H), 4.41 (d, 2H), 4.08 (m, 22H), 3.39 (s, 33H).

Subsequently, the three block copolymers (BCPs) were synthesized using the obtained POEGMA as a macro-CTA through RAFT polymerization (Scheme S4-6). Notably, the three BCPs are distinguished by the specific LC monomer utilized. When ASSChol was used as the sole monomer, the resulting BCPs are referred to as POEGMA-*b*-PASSChol (**P1**). Furthermore, a three-component diblock copolymer, POEGMA-*b*-P(ASSChol-*r*-A6CChol) (**P2**), was synthesized using ASSChol and A6CChol in a 1:1 M ratio. Additionally, we synthesized POEGMA-*b*-PA6CChol (**P3**) by using A6CChol as the sole monomer in a similar manner.

Taking **P2** as an example, the brief synthetic procedures are described below. POEGMA (99 mg, 0.033 mmol), ASSChol (263 mg, 0.5 mmol) and A6CChol (270 mg, 0.5 mmol) were added into a Schlenk flask under a nitrogen atmosphere. A solution of AIBN (1.1 mg, 0.0067 mmol) in dioxane (0.6 mL) was then added into the mixture through the injection. The flask was degassed with three freeze-pump-thaw cycles and immersed in an oil bath at 80 °C for 5 h. Polymerization was quenched by immersion of flask in liquid nitrogen. The resulting solution was concentrated under vacuum using a rotary evaporator, and copolymer was purified by three dissolution-sedimentation cycles in DCM (0.5 mL × 3) and MeOH (45 mL × 3). Finally, the polymer was dried under vacuum for 24 h (0.22 g, yield: 43 %). ^{1}H NMR (500 MHz, $CDCl_3$): δ (ppm) = 7.97 (d, 2H), 7.53 (t, 1H), 7.35–7.39 (m, 3H), 6.32 (t, 1H), 6.23 (d, 1H), 5.39 (s, 11H), 5.33 (s, 14H), 4.47 (m, 11H), 4.35 (m, 44H), 3.39 (s, 33H), 3.10 (m, 14H), 2.95 (m, 44H).

P1 (0.25g, 47 %). ^{1}H NMR (500 MHz, $CDCl_3$): δ (ppm) = 7.90 (d, 2H), 7.56 (t, 1H), 7.33–7.42 (m, 3H), 6.32 (t, 1H), 6.24 (d, 1H), 5.40 (s, 25H), 3.39 (s, 33H).

P3 (0.23g, 43 %) ^{1}H NMR (500 MHz, $CDCl_3$): δ (ppm) = 7.95 (d, 2H), 7.53 (t, 1H), 7.35–7.40 (m, 3H), 6.32 (t, 1H), 6.23 (d, 1H), 5.33 (s, 24H), 3.39 (s, 33H), 3.10 (m, 24H).

2.3.2. Synthesis of croconaine-based amphiphile (CBA)

The synthetic route of photothermal amphiphile is shown in Scheme S7. Starting from 1-(thiophen-2-yl)piperidine-4-carboxylic acid (SP-COOH) [45], two intermediate products, referred to as SP-Chol and SP-PEG, were synthesized via classic esterification. Finally, these two components were bonded together using croconic acid through a dehydration reaction. The detailed synthetic procedures are described below.

SP-Chol. SP-COOH (1.00 g, 4.73 mmol), cholesterol (2.75 g, 7.10 mmol), EDC (1.36 g, 7.10 mmol), DMAP (0.75 g, 6.15 mmol), and dried DCM (25 mL) were added into a Schlenk flask. The mixture solution was stirring overnight at room temperature. After removal of DCM under vacuum using rotary evaporator, the crude product was purified by column chromatography (hexane/EA = 20/1, v/v) to give white solid compound SP-Chol (1.53 g, yield 56 %). ^{1}H NMR ($CDCl_3$, 500 MHz): δ (ppm) = 6.75 (t, 1H), 6.59 (d, 1H), 6.11 (d, 1H), 5.37 (d, 1H), 4.65 (m, 1H), 3.49 (d, 2H), 2.85 (m, 2H), 2.37 (m, 1H), 2.31 (d, 2H), 2.10–0.64 (m, 45H).

SP-PEG. SP-COOH (1.00 g, 4.73 mmol), PEG (3.38 g, 6.15 mmol), EDCI (1.36 g, 7.10 mmol), DMAP (0.75 g, 6.15 mmol), and dried DCM (30 mL) were added into a Schlenk flask. The mixture solution was

stirring overnight at room temperature. After removal of DCM under vacuum using rotary evaporator, the crude product was purified by column chromatography (DCM/MeOH = 40:1, v/v) to give white solid compound SP-PEG (1.89 g, yield 54 %). ^{1}H NMR ($CDCl_3$, 500 MHz): δ (ppm) = 6.76 (m, 1H), 6.59 (m, 1H), 6.11 (m, 1H), 4.24 (t, 2H), 3.70 (t, 2H), 3.64 (t, 48 H), 3.38 (s, 3H), 2.79 (m, 2H), 2.51 (m, 1H), 2.09–1.83 (m, 45H).

CBA. SP-Chol (0.60 g, 1.03 mmol), SP-PEG (1.15 g, 1.55 mmol) and croconic acid (0.15 g, 1.03 mmol) were dissolved in a mixture of n-butanol and toluene (30 mL, 1:1, v/v), then the mixture solution was stirring at 120 °C for 2 h. After removal of solvent under vacuum using rotary evaporator, the crude product was purified by column chromatography (DCM/MeOH = 30:1, v/v) to give solid compound CBA (0.34 g, 70 %). ^{1}H NMR ($CDCl_3$, 500 MHz): δ (ppm) = 8.91–8.66 (m, 2H), 6.57 (s, 2H), 5.37 (d, 1H), 4.64 (m, 1H), 4.28 (m, 2H), 3.98 (s, 4H), 3.76–3.52 (m, 48H), 3.46 (s, 4H), 3.37 (s, 3H), 2.78–2.59 (m, 2H), 2.36–0.65 (m, 51H).

2.4. Critical micelle concentration

Pyrene was employed as a fluorescence probe to determine the critical micelle concentration (CMC) of the synthesized LC-BCPs. Briefly, 10 μL of a pyrene/acetone solution (1.2×10^{-4} M) was added to an aqueous solution of the micelles, with mass concentrations ranging from 1×10^{-5} to 5×10^{-1} mg/mL, resulting in a final pyrene concentration of 6.0×10^{-7} M. The mixture was allowed to equilibrate at room temperature in the dark for 24 h before measurement. Fluorescence spectra were recorded using a FL spectrometer with an excitation wavelength of 334 nm and a scanning range of 350–450 nm. The fluorescence intensity ratios (I_{394}/I_{374}) were calculated and plotted against the BCP concentration.

2.5. Preparation of polymer micelles and DOX-loaded micelles (P@DOX)

In this work, the micelles were prepared by a classical solvent exchange procedure as reported previously [47]. Briefly, BCPs (2 mg) were dissolved in THF (10 mL), followed by the slowly addition of 10 mL of deionized water (100 μL/min/mL) into the organic solution under mild swirling. The resulting turbid mixtures were then dialyzed against deionized water for other 3 days using a Spectra/Por regenerated resin membrane with a molecular cutoff (MWCO) of 6000–8000. The entire process was performed at 20 °C. DOX-loaded micelles (**P@DOX**) were prepared in a similar manner, except for addition of a DMSO solution of DOX·HCl (5 mg/mL, 0.1 mL) to the original 10 mL THF solutions of BCPs (2 mg).

2.6. Preparation of co-micelles (P-CBA) and DOX-loaded co-micelles (P-CBA@DOX)

The co-micelles of **P-CBA** with a weight ratio of 1:2 was prepared following the similar protocol described above. After addition of deionized water, the mixtures were dialyzed against a mixture of water and THF (volume ratio = 1:1) for 2 days. Subsequently, they were dialyzed against deionized water for an additional 3 days using a Spectra/Por regenerated resin membrane with a molecular cutoff (MWCO) of 6000–8000. Correspondingly, **P-CBA@DOX** were prepared in a similar manner as **P@DOX**.

The DOX content in the micelles was determined by measuring the fluorescence intensity of DOX at 590 nm using a fluorescence spectrometer with excitation at 480 nm, calculated with the DOX calibration curve. The concentration of DOX was calculated using the DOX standard curve. The encapsulation capacity (EC) and encapsulation efficiency (EE) were calculated using equations (1) and (2), respectively.

$$\mathrm{EC}(\%) = \frac{\text{weight of loaded drug}}{\text{weight of loaded drug and micelles}} \times 100\% \quad (1)$$

$$\mathrm{EE}(\%) = \frac{\text{weight of loaded drug}}{\text{weight of drug in feed}} \times 100\% \quad (2)$$

2.7. DOX release behaviors of micelles in phosphate-buffered saline (PBS)

The DOX release profiles of the DOX-loaded micelles were examined at 37 °C using a dynamic dialysis method. First, 2 mL of the DOX-loaded micelle suspension was poured into a Spectra/Por regenerated resin membrane dialysis tubing (MWCO = 6000–8000), which was immersed in 20 mL of PBS buffer (pH = 7.4; 0, 10, 30, and 50 mM GSH) with gentle shaking. At predetermined time points, 0.5 mL of the release medium was sampled for fluorescence (FL) analysis and replaced with an equal volume of fresh medium. The release of DOX *in vitro* was routinely analyzed using a FL spectrometer.

To examine NIR laser-triggered drug release, DOX-loaded micelles were evaluated following NIR laser irradiation (808 nm, 1.5 W/cm^2, 5 min) at different irradiation time points (0, 3, 5, and 8 h). Subsequently, the release of DOX was evaluated according to the aforementioned method.

2.8. In vitro photothermal effect

Suspensions of **CBA** and CBA-containing micelles were added to quartz cells and then exposed to NIR laser irradiation (808 nm, 1.5 W/cm^2) until the photothermal temperature reached a plateau. The increase in the temperature of each sample during this process was recorded using an infrared thermal imaging system.

2.9. Cell culture

Human cervical adenocarcinoma HeLa cells were acquired from the cell library of the Chinese Academy of Sciences and cultured in Dulbecco's Modified Eagle's Medium (DMEM) supplemented with 10 % fetal bovine serum (FBS) and 1 % antibiotics (penicillin–streptomycin) at 37 °C under 5 % CO_2. The cells were subcultured every 2–3 days using trypsin.

2.10. In vitro cytotoxicity

The cytotoxicity of BCP micelles and CBA was assayed in HeLa cells using the CCK-8 assay kit. The HeLa cells were first seeded into 96-well microplates (1×10^4 cells/well) containing DMEM supplemented with 10 % FBS and 1 % antibiotics (penicillin–streptomycin). After 24 h of incubation, the medium was aspirated and replaced with 100 μL of fresh medium containing various concentrations of BCP micelles or CBA (10, 20, 50, 80, 100, 150, and 200 μg/mL). Then, the cells were cultured at 37 °C under 5 % CO_2 for another 24 h. Subsequently, the culture medium in the wells was replaced with 100 μL of fresh medium containing 10 μL of the CCK-8 reagent. After 2 h of incubation, the absorbance of each well at 450 nm was detected using a microplate reader (SpectraMax M2e, Molecular Devices). Finally, the relative cell viability was evaluated using eq. (3) (n = 4).

$$\text{Relative cell viability } (\%) = \frac{\mathrm{OD}_{450}(\text{sample}) - \mathrm{OD}_{450}(\text{blank})}{\mathrm{OD}_{450}(\text{control}) - \mathrm{OD}_{450}(\text{blank})} \times 100\% \quad (3)$$

Similarly, the cytotoxicity of DOX-loaded micelles was also examined in HeLa cells using the CCK-8 assay kit. DOX-loaded micelles and free DOX were added to fresh medium to achieve final DOX concentrations of 0.1, 0.5, 1, 2, 5, 10, and 20 μg/mL. The remaining procedure was the same as that described above.

2.11. Preparation of FITC-labeled micelles and co-micelles

Fluorescein-5-maleimide (Mal-FITC, 5 mg) was dissolved in DMSO

(1 mL), then 10 μL of this solution was added to 5 mL of micelles formed by P2 or co-micelles formed by P2-CBA. The mixtures were stirred for 12 h at room temperature. The turbid mixtures were then dialyzed against deionized water for an additional 3 days to remove unreacted Mal-FITC, using a Spectra/Por regenerated resin membrane with a molecular cutoff (MWCO) of 6000–8000.

2.12. Cell uptake assay

HeLa cells were seeded into confocal culture dishes (1×10^4 cells/well) in DMEM supplemented with 10 % FBS and 1 % antibiotics (penicillin–streptomycin). The cells were incubated with FITC-modified micelles for 4 h at 37 °C. After the removal of culture medium, the cells were fixed with 4 % paraformaldehyde (PFA) for 15 min and rinsed with PBS. The cell nuclei were stained with 4′,6-diamidino-2-phenylindole (DAPI) for 10 min in the dark. The cells were finally observed using an LSM 710 confocal laser scanning microscope (CLSM, Zeiss, Germany).

2.13. Intracellular DOX release and photothermal effects

Intracellular DOX release and photothermal effects were examined in HeLa cells using fluorescence microscopy. First, the cells were cultured on coverslips placed in 48-well plates (1×10^4 cells/well) in DMEM containing 10 % FBS and 1 % antibiotics (penicillin–streptomycin). The cells were incubated with various micelles for 24 h at 37 °C. After the culture medium was removed, the cells were rinsed thrice with PBS and stained using the Calcein-AM/PI Double Staining Kit. Fluorescence images were then recorded using an Olympus CKX-53 fluorescence microscope. Additionally, the relative cell viabilities of HeLa cells incubated with CBA-contained co-micelles and subjected to NIR laser irradiation (808 nm, 1.5 W/cm^2) were also examined using a CCK-8 assay kit, as described previously.

To further evaluate the photothermal cytotoxicity of CBA-contained co-micelles, eBioscience™ Annexin V Apoptosis Detection Kit (Invitrogen™, Carlsbad, CA, USA) was used. HeLa cells were cultured on coverslips placed in 6-well plates (5×10^5 cells/well). After different treatment, cells were harvested, washed three times with cold PBS, and resuspended in 100 μL binding buffer. Then the cells were stained with Annexin V-APC and PI, and incubated for 15 min in the dark. Finally, the stained cells were analyzed by a flow cytometer (Beckman, Indianapolis, United States).

2.14. Animal models

All mouse experiments were carried out in accordance with the guidelines of the Institutional Animal Care and Use Committee (IACUC) of Shanghai Laboratory Animal Research Center (Authorization numbers: 202,400,802). 6-weeks-old male BALB/c nude mice (17−20 g) were purchased from Zhejiang Vital River Laboratory Animal Technology Co., Ltd. [SCXK(Zhejiang)2024–0001]. The mice were kept in the SPF facility with a temperature range of 20–26 °C and a relative humidity of 40–70 %. HeLa cells (1×10^6) were inoculated subcutaneously into the right flanks of the mice. The tumor-bearing mice were used for experiments after the tumor size grew to about 100 mm^3.

2.15. In vivo imaging

For *in vivo* imaging, 200 μL of **P2-CBA** co-micelles were injected into tumor-bearing BALB/c nude mice via the tail vein (**CBA**, 1.5 mg/kg). Then, *in vivo* fluorescence imaging was performed at 0, 0.5, 1, 2, 4, 6, 8, 24, 48, and 72 h post-injection using a BLT *in vivo* imaging system (AniView 100). Tumors and normal organs including the heart, liver, spleen, lung, and kidney were also collected from some tumor-bearing nude mice at 2 h post-injection and observed using BLT *in vivo* imaging system (AniView 100).

For *in vivo* photothermal imaging, at 2 h post-injection, the tumor sites were irradiated with a laser (808 nm, 1.5 W/cm^2). Then, photothermal images were obtained during laser irradiation using an infrared thermal imaging system. Mice treated with PBS were used as the control.

2.16. In vivo antitumor efficacy

For the examination of *in vivo* antitumor effects, tumor-bearing BALB/c nude mice were randomly divided into six groups (four mice per group): PBS, **P2@DOX**, **P2-CBA@DOX**, free DOX, **P2-CBA + Laser**, and **P2-CBA@DOX + Laser**. When the tumor sizes reached ~100 mm^3, these mice received intravenous injections of various micelles according to their treatment groups. At 2 h post-injection, the tumors of mice in the NIR treatment groups were treated with 808 nm NIR laser irradiation (1.5 W/cm^2, 5 min). The injections and laser treatments were administered on day 0, day 3, and day 6. The body weight and tumor sizes of the mice were measured every 3 days after treatment. Tumor volume was calculated as follows: Tumor volume = AB^2*0.5, where A is the longer and B is the shorter diameter (mm). The tumors were excised and weighed after 30 days for assessing the antitumor efficacy of the different treatments. The tumor tissues and main organs were also fixed with 4 % PFA and stained with hematoxylin and eosin (H&E) for histopathological analysis. To observe proliferation of tumor cells and angiogenesis, the apoptosis of tumor cells, tumor sections were stained with anti-Ki67, anti-CD31, and Caspase-3 (Abcam, Cambridge, MA, USA) followed by HRP-conjugated affinipure goat anti-rabbit IgG (H + L).

2.17. Statistical analysis

All data were representative of at least four independent experiments and were represented as the mean ± standard deviation (SD). Significant differences between various groups were calculated using Student's t-tests with GraphPad Prism software. $p < 0.05$ was considered statistically significant and denoted using the * symbol, while ** and *** indicated $p < 0.01$ and $p < 0.001$, respectively.

3. Results and discussion

3.1. Synthesis and characterization of LC-BCPs

In this study, the three block copolymers POEGMA-*b*-PASSChol, POEGMA-*b*-P(ASSChol-*r*-A6CChol), and POEGMA-*b*-PA6CChol are referred to as **P1**, **P2**, and **P3**, respectively (Fig. 1a). Their chemical structures, molecular weights, and polydispersity indexes (*Đ*) were characterized ^{1}H NMR and GPC (Figs. S4–7). Notably, the design of the hydrophobic blocks ensured that they had the same degree of polymerization in order to facilitate subsequent comparative experiments. The degree of polymerization in each block of the BCPs was labeled via subscripts, as follows: $POEGMA_{11}$-*b*-$PASSChol_{25}$, $POEGMA_{11}$-*b*-P($ASSChol_{11}$-*r*-$A6CChol_{14}$), and $POEGMA_{11}$-*b*-$PA6CChol_{24}$. Specifically, characterization experiments on **P2** indicated that the ASSChol units ($DP_{ASSChol} = 11$) were slightly fewer in number than the A6CChol units ($DP_{A6CChol} = 14$), with both these units appearing in the hydrophobic block of **P2** in a random manner. The results are summarized in Table S1.

Cholesterol-based polymers are considered typical liquid crystalline polymers. In these polymers, the rigid cholesterol mesogens are often arranged in a tail-to-tail manner, forming a smectic A phase. Consistent with previous reports [48,49], in the bulk state, the synthesized BCPs exhibited liquid crystallinity, as evidenced by small angle X-ray scattering (SAXS) experiments. As shown in Fig. 1b, **P1** and **P2** exhibited sharp scattering peaks at 1.55 nm^{-1} and 1.53 nm^{-1}, with corresponding calculated *d*-spacing values of 4.05 nm and 4.10 nm, respectively. This indicated that both these BCPs exhibited an interdigital smectic A phase (SmA_d), which was further confirmed by the typical fan texture observed using polarized optical microscopy (POM) (Fig. 1c–e). In contrast, **P3**

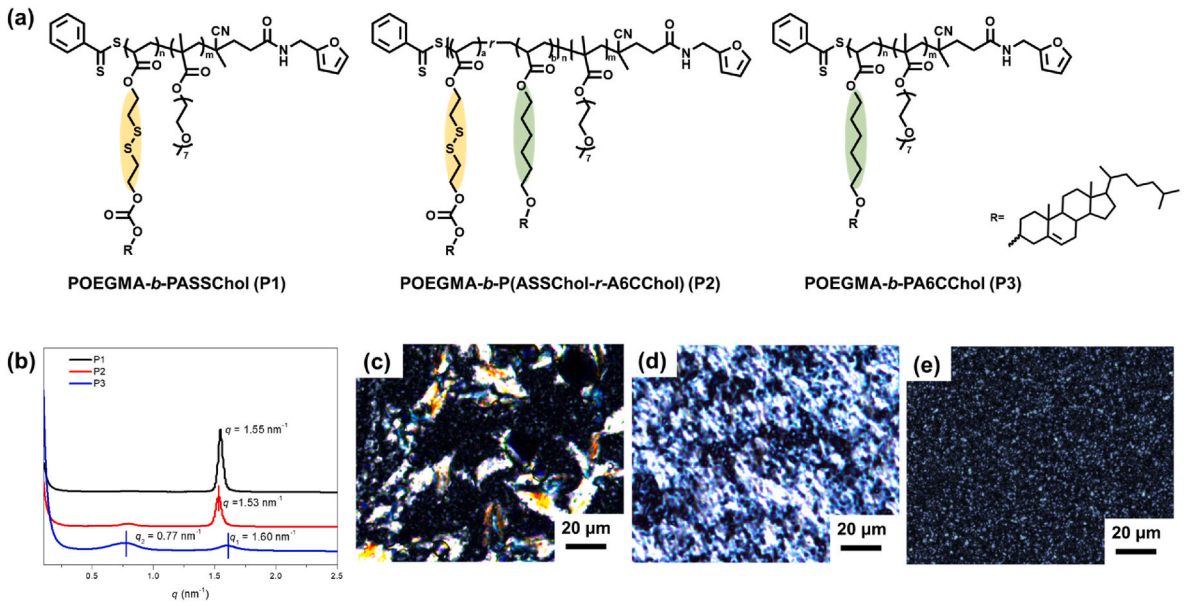

Fig. 1. (a) Chemical structures and (b) SAXS intensity curves of the three BCPs. Polarized optical microscopy (POM) images of (c) P1, (d) P2, and (e) P3 during the cooling process.

showed two broad diffraction peaks at 0.77 nm^{-1} and 1.60 nm^{-1}, which suggested that it exhibited a nematic phase and underwent microphase separation under bulk conditions. These results demonstrated that the introduction of disulfide bonds into the side chains of hydrophobic blocks increases the LC ordering of mesogens, likely due to the improved decoupling effect of heteroatoms. The LC-isotropic phase transition temperature (T_{LC-I}), determined using differential scanning calorimetry (DSC) (Fig. S8), was the highest in **P1**, followed by **P2** and **P3**, further supporting this observation.

3.2. Reduction-triggered degradation of LC-BCPs

To assess the reduction response of the BCPs, we first performed GPC on the BCPs dissolved in THF after adding the reducing agent GSH (10 mM). As depicted in Fig. 2a and **b**, the GPC peaks of **P1** and **P2**, which contained disulfide bonds in their pendant groups, showed a significant shift towards a lower molecular weight at 6 h after GSH addition. This suggested that 10 mM GSH could effectively cleave the disulfide bonds in the side chains of BCPs in THF, inducing the detachment of rigid cholesterol fragments from the polymer and consequently decreasing the molecular weight. Additionally, when the GPC curves of **P1** and **P2** were compared, a certain amount of residual **P1** was detected at the end of the observation period, while **P2** essentially showed complete degradation. This difference could be attributed to the content of disulfide bonds, which was approximately twice as high in **P1** as in **P2**. After 24 h of incubation with GSH, both solutions exhibited additional right-shift GPC peaks corresponding to lower molecular weights. Notably, the change in the elution peak of **P1** (1.3 min) was larger than that of **P2** (1.1 min), consistent with the fact that A6CChol units were still present in **P2**. Furthermore, the GPC curves of **P3** — which did not

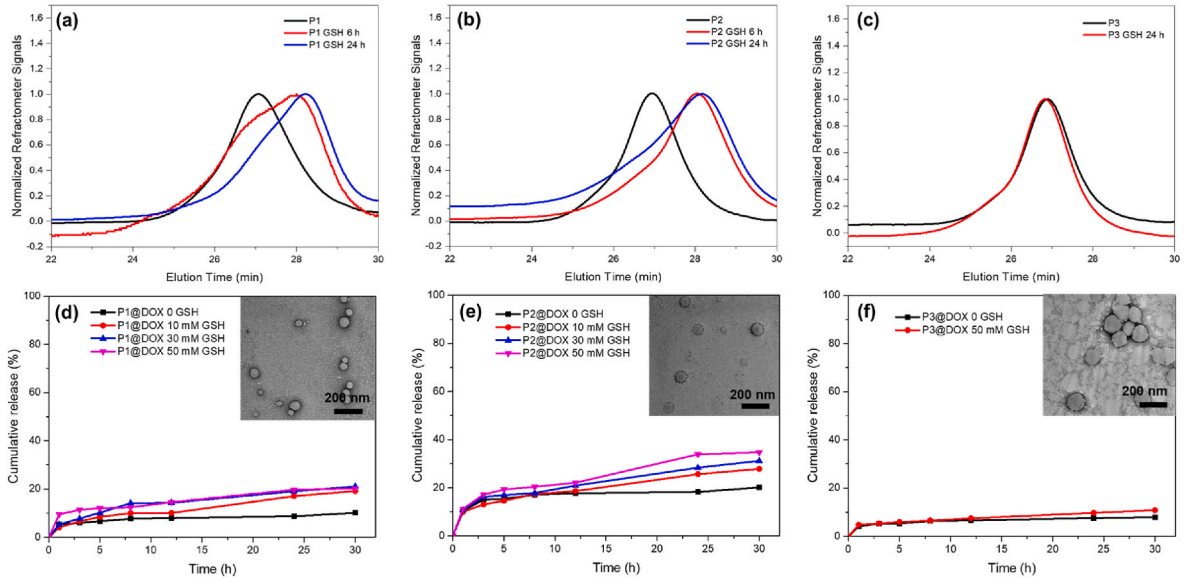

Fig. 2. GPC curves of (a) P1, (b) P2, and (c) P3 before and after the addition of GSH. GSH (10 mM) was added to copolymers dissolved in THF, and the solutions were analyzed after 6 h and 24 h following GSH addition. DOX release profiles of (d) P1@DOX, (e) P2@DOX, and (f) P3@DOX in PBS containing different concentrations of GSH. Insets show TEM images of DOX-loaded micelles formed by P1, P2, and P3.

contain disulfide bonds — showed almost no change even 24 h after GSH addition (Fig. 2c). These results indicated that incorporating disulfide bonds in the side chains of polymers provides an excellent reduction-triggered degradation response in LC-BCPs.

3.3. Preparation of DOX-loaded micelles and drug release behavior

To confirm the potential of the synthesized LC-BCPs as efficient carriers for drug delivery, we conducted an analysis of their critical micelle concentrations (CMCs) in aqueous environments, utilizing pyrene as a fluorescent indicator. As depicted in Fig. S9, the three LC-BCPs exhibited exceptionally low CMCs ranging from 0.0005 to 0.0016 mg/mL. These findings suggest that these micelles possess exceptional post-administration stability, even in the highly diluted conditions encountered within the blood circulation system. DOX-loaded polymeric micelles (**P@DOX**) were prepared via the solvent exchange method [50]. The detailed protocol is described in the experimental section. As shown in the transmission electron microscopy (TEM) images in Fig. 2d–f, DOX-loaded polymer micelles (**P1@DOX**, **P2@DOX**, and **P3@DOX**) had typical spherical structures with average diameters of 190, 150, and 210 nm, respectively, smaller to the spherical micelles formed by the corresponding BCPs (Fig. S10). The encapsulation capacity (EC) and encapsulation efficiency (EE) of these micelles are summarized in Table S2. Compared to **P3** (EC = 0.44 %, EE = 2.15 %), **P1** and **P2** demonstrated relatively higher EC (1.51 %, 1.93 %) and EE values (7.11 %, 8.94 %). Hence, the introduction of disulfide bonds in the hydrophobic blocks promoted the encapsulation of DOX. Interestingly, the highest EC and EE were observed in **P2@DOX**. This suggests that a moderate degree of ordered arrangement facilitates the embedding of DOX, while a highly ordered LC phase arrangement reduces the encapsulation efficiency of DOX.

DOX release from the three **P@DOX** micelles was explored by incubating these micelles with GSH in PBS buffer (pH 7.4) and monitoring DOX release with a fluorescence spectrometer. The cumulative release of DOX as a function of time is presented in Fig. 2d–f. Unlike the cleavage of disulfide bonds in dissolved polymer chains, which primarily depends on pH [51], temperature [52,53], and reduction agent [54], the reduction-triggered release behavior of the micelles was also influenced by their aggregation state [55]. After 30 h of incubation in the absence of GSH, the three types of DOX-loaded micelles showed a minimal leakage of encapsulated DOX in PBS buffer. In contrast, when incubated with GSH, they exhibited noticeable drug release, except for **P3@DOX**, with cumulative release increasing as GSH concentrations increased from 10 to 50 mM. However, the cumulative release of DOX from **P1@DOX** and **P2@DOX** micelles was relatively low compared to previous reports at the same GSH concentrations [56]. Even at high concentrations of GSH (50 mM), both types of micelles exhibited release percentages of approximately 20.2 % and 34.7 %, respectively. This release behavior was closely related to the LC arrangement of PAChol blocks in the micelles, which provided a physical cross-linking effect and thus slowed down the disaggregation of micelles [57]. This LC ordering effect had a crucial effect on the release behavior of the micelles, surpassing the influence of disulfide bond content. **P1** had a consistent LC block structure consisting of ASSChol mesogens throughout, and theoretically, it should have been more sensitive to GSH. However, **P2@DOX** exhibited higher DOX release than **P1@DOX**. This difference could be attributed to the moderate LC ordering in **P2** due to the random polymerization conformation of ASSChol and A6CChol in its LC block. Nevertheless, the introduction and regulation of LC ordering represented an alternative approach for achieving controlled drug release, ensuring the significant stability of carrier materials and limiting drug leakage in plasma during prolonged blood circulation.

3.4. Synthesis and characterization of the photothermal amphiphile

To achieve photo-chemotherapy, we synthesized a croconaine-based amphiphile, referred to as **CBA**, which served as a photothermal agent. Croconaine-based dyes are characterized by an electron donor–acceptor–donor (D–A–D) type pseudo-oxocarbon structure, which ensures intense absorption in the NIR region and high photothermal conversion efficiency [58,59]. Additionally, we introduced PEG (M_n = 550) and cholesterol moieties on the two sides of the croconaine center (Fig. 3a). The details of CBA synthesis and the corresponding ^{1}H NMR spectra are provided in the Supplementary Information (Scheme S7, Figs. S11–13). Our design aimed to increase the water solubility of **CBA** via the PEG chain. More importantly, our recent research showed that both cholesterol moiety-containing LC-BCPs and amphiphiles can undergo synergetic co-assembly to generate stable hierarchical co-micelles [46].

The optical properties of **CBA** in solution were investigated using UV/vis spectroscopy. As shown in Fig. 3a, **CBA** dissolved in dimethyl sulfoxide (DMSO) exhibited a maximum absorption peak at $\lambda_{max\text{-}DMSO}$ = 795 nm, consistent with previously reported croconaine-based NIR dyes [20]. As depicted in Fig. 3b and c, CBA also exhibited significant photothermal properties. After 10 min of irradiation with an NIR laser (808 nm, 1.5 W/cm^2), the solution reached a plateau photothermal temperature (T_{max}) of 79.6 °C. The photothermal conversion efficiency (η) of CBA in DMSO was calculated to be 66.4 % (Fig. S14) [60]. The photothermal properties of **CBA** remained unchanged after multiple laser irradiation cycles (Fig. 3d), demonstrating the photothermal stability of this amphiphile.

3.5. Preparation of co-micelles and their photothermal effects

Considering its high stability and efficient drug release performance, we selected **P2** as the optimal LC-BCP candidate for further research. The co-micelle composed of P2 and CBA with an optimized weight ratio of 1:2, designated as **P2-CBA**, was prepared using the described protocol in experimental section. The CMC value of **P2-CBA** was measured at 0.0012 mg/mL (Fig. S15), which is similar to that of **P2** (Fig. S9). Interestingly, **P2-CBA** micelles demonstrated uniform and prominent vesicular structures, with their average diameter decreasing to 112 nm (Fig. 4a). The average thickness of the membrane in these micelles was measured to be 12.5 nm. This indicated that the amphiphiles were embedded within the membrane core, thereby increasing the packing parameter to $1/2 \leq p < 1$, which facilitated the formation of vesicular co-micelles [61]. This vesicular structure was highly flexible and was capable of further encapsulating drug molecules, especially hydrophilic ones. The semiquantitative embedding efficiency, calculated using a **CBA** calibration curve (Fig. S16), was found to be 34.5 % under a **CBA** feed concentration of 0.4 mg/mL. Specifically, 1 mg of the co-micelles contained 0.412 mg **CBA**, indicating that **CBA** had become a key component of the co-micelle framework. The co-assembly process enabled the **CBA** in the **P2-CBA** to exhibit a broad UV/Vis absorption band ranging from 610 to 900 nm (Fig. S17a). This suggested that **CBA** was embedded within the co-micelles in both H-aggregated and J-aggregated forms. As depicted in Fig. 4b, under laser irradiation (808 nm, 1.5 W/cm^2) for 15 min, the **P2-CBA** (C_{CBA} = 0.5 mg/mL) exhibited remarkable photothermal performance (T_{max} = 65.6 °C). Interestingly, TEM showed that the vesicular morphology of the co-micelles was retained, with only a slight decrease in size observed after NIR laser irradiation (Fig. S17b). This indicated that the co-micelles demonstrated remarkable stability, which was likely due to the LC arrangement in their core. The tight embedding of **CBA** within the co-micelles restricted its leakage post-irradiation, thereby minimizing potential risks *in vivo*.

3.6. Photothermal reduction-triggered release behavior of DOX-loaded co-micelles

DOX-loaded **P2-CBA@DOX** co-micelles, with a P2-to-CBA feed weight ratio of 1:2, were prepared using the same protocol for preparing **P2@DOX**. As shown in Fig. 4c, **P2-CBA@DOX** co-micelles appeared as

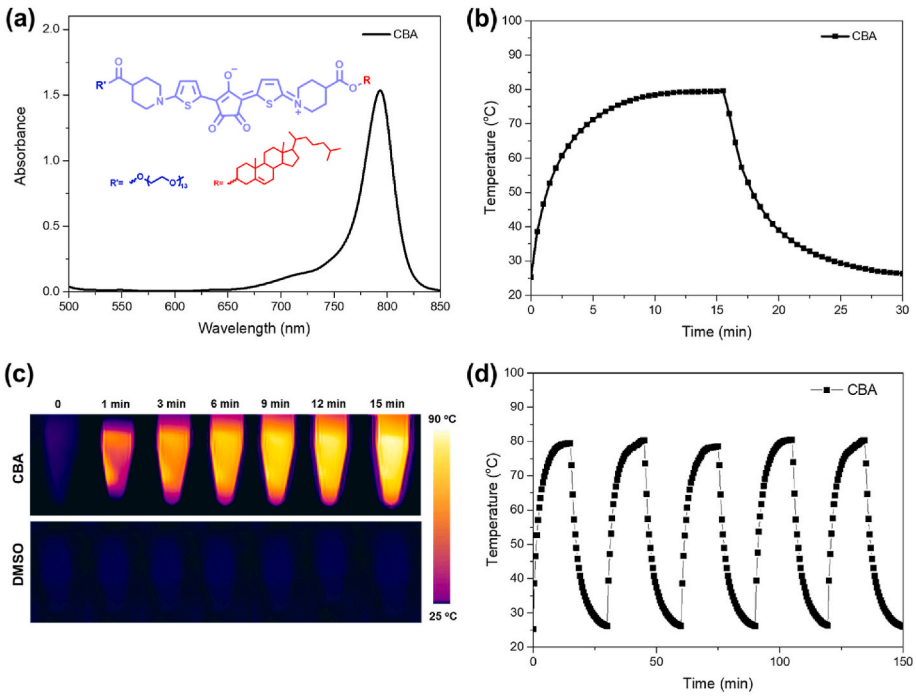

Fig. 3. (a) UV/vis absorption spectra of CBA in DMSO (0.02 mg/mL). (b) Photothermal heating curves, (c) infrared thermal images, and (d) photothermal stability of CBA (0.2 mg/mL) following NIR laser irradiation (808 nm, 1.5 W/cm^2).

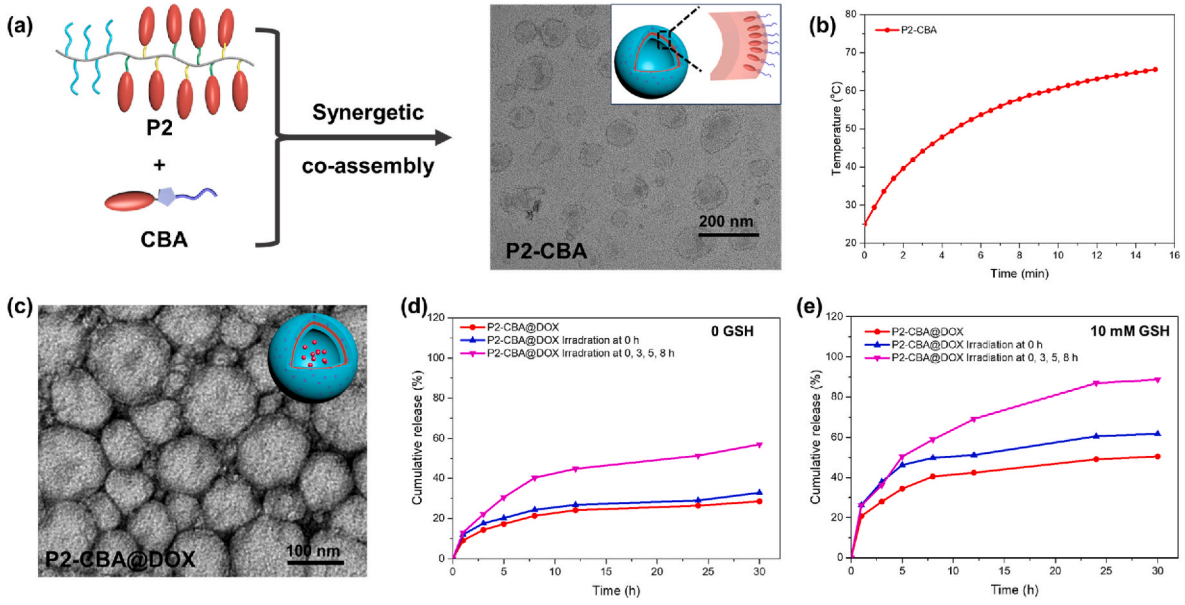

Fig. 4. (a) Schematic illustration and TEM image of co-micelles formed by P2 and CBA. (b) Photothermal heating curves of P2-CBA upon laser irradiation (808 nm, 1.5 W/cm^2). (c) TEM image and schematic illustration of P2-CBA@DOX. *In vitro* DOX release profiles of P2-CBA@DOX (d) in the absence and (e) presence of 10 mM GSH in PBS (pH = 7.4).

spherical vesicles, and the membrane thickness of these co-micelles was noticeably increased to ~32 nm. The EE and EC of DOX in **P2-CBA@DOX** were approximately double those in **P2@DOX** (Table S2). This significant improvement was attributed to the encapsulation of DOX both within the membrane and in the interior of the vesicles. However, the content of embedded **CBA** in **P2-CBA@DOX** was slightly lower (~25.6 %) than that in **P2-CBA**, possibly due to the presence of DOX. The drug release behavior of **P2-CBA@DOX** was then studied under various conditions, including the presence/absence of GSH and NIR laser irradiation. When GSH was absent, **P2-CBA@DOX** exhibited minimal spontaneous leakage (~20 %), similar to **P2@DOX** in the absence of NIR laser irradiation (Fig. 4d). This suggested that the incorporation of **CBA** within the polymeric micelles did not significantly affect their structural stability. When the **P2-CBA@DOX** solution was exposed to 5 min of irradiation (808 nm, 1.5 W/cm^2), only a slight (5 %) increase in cumulative release was observed (blue line in Fig. 4d). Notably, a single round of irradiation could increase the solution temperature to 51 °C within 5 min, and the corresponding increase in drug release was attributed to heat-induced acceleration of drug diffusion during the irradiation period. Subsequently, without further irradiation,

the temperature increase did not contribute further to the cumulative drug release. After the solution was irradiated multiple times (each for 5 min) at time points of 0, 3, 5, and 8 h, the cumulative release at 8 h reached 40.3 % (purple line in Fig. 4d). This indicates that the cumulative release of DOX is influenced by the frequency of irradiation, and multiple exposures can enhance the release rate to a certain extent.

In the presence of GSH, a significant increase in the cumulative release of DOX from **P2-CBA@DOX** was observed (Fig. 4e), particularly following NIR laser irradiation. Notably, in **P2@DOX**, which showed low reduction-responsiveness due to its ordered LC arrangement and consequent tight micellar structure, the cumulative drug release rate only reached 34.7 % even after 30 h of incubation in PBS (pH = 7.4) containing 50 mM GSH. In contrast, **P2-CBA@DOX** exhibited a 51.2 % cumulative drug release rate at a GSH concentration as low as 10 mM (red line in Fig. 4e). This indicated that co-assembly with **CBA** effectively modulated the LC ordering effect within the co-micelles, as also evidenced by the SAXS profile (Fig. S17c), thereby enhancing the reaction between GSH and disulfide bonds and accelerating drug release. Furthermore, when the **P2-CBA@DOX** solutions incubated in the presence of GSH (10 mM) were exposed to one round of NIR laser irradiation (1.5 W/cm^2, 5 min), an approximate 11.3 % increase in cumulative drug release was observed (blue line in Fig. 4e). This increase was twice that observed under pure lighting conditions (blue line in Fig. 4d). Noteworthy, four rounds of NIR laser irradiation (1.5 W/cm^2, 5 min) at 0, 3, 5, and 8 h resulted in a nearly 90 % cumulative release of DOX. This outcome clearly indicated that the heat produced by **CBA** upon laser irradiation not only improved the diffusion of drug molecules but also accelerated the disruption of disulfide bonds. This demonstrated the feasibility of precisely tuning the release of DOX based on photothermal conversion effects using **P2-CBA@DOX** co-micelles, which could be tailored to meet synergetic therapeutic needs.

3.7. *In vitro evaluation of synergistic cytotoxicity*

The cytocompatibilities of the micelles formed by the three BCPs and **CBA** were first evaluated in HeLa cells using CCK-8 assays. As illustrated in Fig. 5a, the BCP micelles exerted negligible cytotoxicity. After 24 h of incubation, the cell viability remained almost 100 % even at high BCP micelle concentrations (200 μg/mL). This indicated that the reduction-responsive LC-BCPs developed in this study possessed excellent biocompatibility, regardless of the disulfide bond content in their LC blocks. Additionally, **CBA** also exhibited excellent biocompatibility, although the cell viability decreased to 81 % in the presence of high **CBA** concentrations of 200 μg/mL. Nevertheless, the cytotoxicity of **CBA** was much lower than that of commonly used NIR dyes [21]. This was due to the specific chemical structure of **CBA**, which bore biocompatible PEG and cholesterol moieties on both sides of its croconaine center.

To explore the cellular uptake of micelles, FITC-labeled **P2** micelles and **P2-CBA** co-micelles were initially prepared by utilizing the furan group present at the end of the hydrophilic block of **P2**. This group was introduced using a furan-functionalized chain transfer agent (CTA) during polymerization, allowing reactions with maleimide derivatives through a Diels-Alder (D-A) reaction [62,63]. Notably, this convenient and effective *in-situ* modification method in aqueous medium enables the modification of micellar surfaces with various functional groups, including proteins and biomolecules. Accordingly, FITC grafting rates of 46 % and 52 % were obtained for **P2** micelles and **P2-CBA**, respectively, as calculated using Mal-FITC calibration curves (excitation wavelength, EX = 490 nm). Subsequently, HeLa cells were incubated with the two types of FITC-labeled micelles for 4 h, and their nuclei were then stained with DAPI. Confocal laser scanning microscopy (CLSM) revealed distinct green fluorescence ascribed to FITC-labeled micelles in both the cytoplasm and the nuclei of HeLa cells post-incubation (Fig. 5b). Merged images displayed a light blue color within the nuclei, suggesting that there was an overlap of green fluorescence (FITC-labeled micelles) and blue fluorescence (from DAPI-stained nuclei). This indicated that both types of micelles had indeed been translocated to the nuclei of the HeLa cells.

Furthermore, the cytotoxicity of free DOX, **P2@DOX**, and **P2-CBA@DOX** was evaluated across various DOX concentrations (ranging from 0.1 to 20 μg/mL) using a CCK-8 assay (Fig. 5c). After incubation with HeLa cells for 24 h, free DOX demonstrated significant cytotoxicity, with the cell viability dropping below 14 % at a DOX concentration of 5 μg/mL, likely due to its direct diffusion into cell nuclei. In contrast, both DOX-loaded micelles showed relatively lower cytotoxicity. However, when HeLa cells were treated with **P2-CBA@DOX** at higher DOX concentrations (10 and 20 μg/mL), a notable decrease in cell viability was detected. This indicated that the upper limit of tolerated DOX concentrations under encapsulated conditions was approximately 5 μg/mL. The reduction in viability at higher DOX concentrations could be attributed to the efficient intracellular reduction-triggered release of DOX from **P2-CBA@DOX**, leading to a cumulative release effect exceeding the tolerance limit of the cells. Consequently, **P2-CBA@DOX** with a DOX concentration of 5 μg/mL was chosen for subsequent experiments.

Finally, the *in vitro* synergistic therapeutic effects of **P2-CBA@DOX** were further investigated. HeLa cells were co-incubated with **P2-CBA@DOX** for 4 h and then exposed to an NIR laser (808 nm, 1.5 W/cm^2) for various durations (0, 0.5, 1, 1.5, 2, 2.5, and 3 min). Then, cell viability was explored using CCK-8 assays at 0.5 h and 24 h post-treatment. As shown in Fig. 5d, the cell viability decreased gradually as the irradiation time was prolonged. Notably, after 3 min of irradiation, approximately 95 % of HeLa cells were inactivated after both 0.5 h and 24 h due to significant temperature increases (Fig. S18). However, compared to the 0.5 h incubation groups, the 24 h incubation groups exhibited relatively lower cell viability following 3 min of irradiation. For example, 1.5 min of irradiation induced 53 % and 84 % cell death in the 0.5 h and 24 h incubation groups, respectively. This indicated that the heat generated by NIR laser irradiation caused cell death while also accelerating DOX release from the co-micelles. After irradiation was ceased, the heating stopped. However, the released DOX continued to inactivate the cells, resulting in a further decrease in cell survival during the 24 h incubation period. The live/dead staining results (Fig. 5e) were consistent with the results of the CCK-8 assay, visually revealing the *in vitro* death of HeLa cells.

To quantitatively assess the synergistic effect of photothermal therapy combined with chemotherapy in inducing cell death, we employed the Bliss Independence Model [64], which calculates the expected combined effect under the assumption that each treatment acts independently. First, the cell death rates were measured for HeLa cells treated with photothermal therapy alone (P2-CBA + Laser), chemotherapy alone (P2-CBA@DOX) and the combined treatment (P2-CBA@DOX + Laser). The theoretical combined effect ($E_{theoretical}$) was calculated using the Bliss formula: $E_{theoretical} = E_A + E_B - E_A * E_B$, where E_A represents the cell death rate from photothermal therapy alone, and E_B represents the cell death rate from chemotherapy alone. The observed cell death rate from the combined treatment (E_{actual}) was then compared to the theoretical combined effect ($E_{theoretical}$). A synergistic effect is indicated if $E_{actual} > E_{theoretical}$, an additive effect if $E_{actual} = E_{theoretical}$, and an antagonistic effect if $E_{actual} < E_{theoretical}$.

In the study, the photothermal therapy alone (P2-CBA + Laser) yielded a cell necrosis rate of $E_A = 81.50$ %, and chemotherapy alone (P2-CBA@DOX) yielded a cell necrosis rate of $E_B = 27.10$ % (Fig. 5f). For the combined treatment (P2-CBA@DOX + Laser), the observed cell apoptosis rate was $E_{actual} = 91.10$ %. Converting to decimal values ($E_A = 0.815$, $E_B = 0.271$) and substituting into the Bliss formula, we obtained $E_{theoretical} = 0.815 + 0.271 - (0.815 * 0.271) = 0.8651$, which converts to $E_{theoretical} = 86.51$ %. Comparing the observed and theoretical effects, the actual cell death rate of 91.10 % slightly exceeded the theoretical rate of 86.51 %, suggesting a potential synergistic effect. This substantial difference indicates that the effectiveness of the combined treatment significantly increased compared with the simple sum of their individual effects, supporting a significant synergistic effect exists when

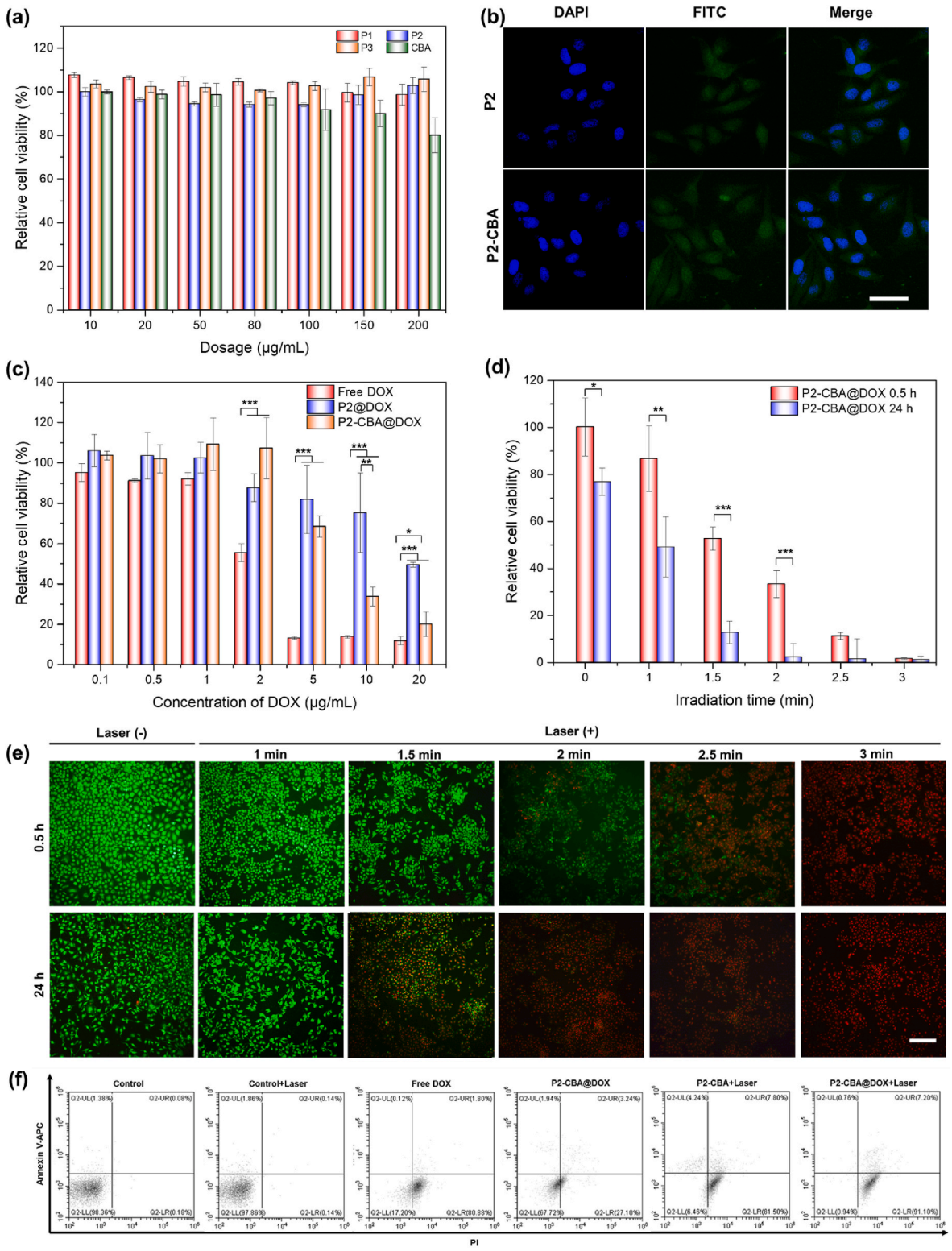

Fig. 5. (a) Relative viability of HeLa cells after 24 h of incubation with various concentrations of copolymers and CBA. (b) CLSM images of HeLa cells showing the cellular uptake of FITC-labeled P2 micelles and P2-CBA co-micelles after 4 h. Scale bar = 40 μm. (c) Relative viability of HeLa cells incubated for 24 h with DOX-loaded micelles and free DOX at different DOX dosages. (d) Relative viability of HeLa cells under different treatment conditions. (e) Live/dead staining of HeLa cells under different treatment conditions. Green represents live cells, while red represents dead cells. Scale bar = 100 μm. (f) Flow cytometer analysis of cell apoptosis gating on Annexin V-APC/PI staining. Data are expressed as the mean ± SD (n = 4, *$p < 0.05$; **$p < 0.01$; ***$p < 0.001$).

photothermal therapy and chemotherapy are combined. Although DOX may have shown a limited contribution to the outcomes of this combination therapy system, its toxic side effects were also minimized in this system. Moreover, the presence of DOX provided effective secondary treatment for tumor cells that survived after NIR laser irradiation, thereby enhancing the overall efficacy of the dual treatment approach.

3.8. Biodistribution and in vivo imaging

The *in vivo* biodistribution of **P2-CBA** in tumor-bearing BALB/c nude mice was first explored using NIR fluorescence imaging. Free **CBA** and **P2-CBA** co-micelles exhibited significant NIR fluorescence emission at 815 nm when excited at 780 nm (Fig. S19), consistent with the excellent real-time bioimaging capacity of croconaine-based dyes reported previously [20]. Following the intravenous injection of **P2-CBA**, a clear fluorescence signal was observed at tumor sites within 0.5 h (Fig. 6a). The fluorescence intensity within the tumor peaked rapidly at just 2 h post-injection, demonstrating the efficient targeting and accumulation of the co-micelles at tumor sites. Notably, the fluorescence signal intensity showed only a slight decrease within 8 h post-injection, demonstrating that **P2-CBA** also has a long retention time within tumor tissues. Although a progressive decrease in fluorescence signals was observed over time, the obvious intratumoral accumulation of **P2-CBA** remained evident even at 72 h post-injection. Additionally, some mice were sacrificed at 2 h post-injection, corresponding to the peak of fluorescence intensity in the whole body. *Ex vivo* imaging further confirmed significant fluorescence signals in tumor tissue, and the major organs (heart, liver, spleen, lung, and kidney) also displayed fluorescence signals due to the diffusion effect (Fig. S20). This distribution pattern is commonly observed after treatment with drug carriers that lack targeting groups [65]. Nevertheless, despite their wide distribution, the micelles showed substantial accumulation at tumor sites, which demonstrated their good passive targeting ability.

Subsequently, we evaluated *in vivo* photothermal conversion effects in mice. Considering that fluorescence peaked at 2 h post-injection (Fig. 6b), NIR laser irradiation (808 nm, 1.5 W cm^2) was administered at 2 h after the intravenous injection of either PBS or **P2-CBA**. Real-time temperature variations were recorded using an infrared thermal camera. As shown in Fig. 6c and d, the tumor sites of mice treated with **P2-CBA** showed notable temperature elevations, with the temperature increasing from 33.5 °C to 52 °C within 5 min. In contrast, mice treated with PBS showed only exhibited a 2.5 °C increase in the tumor site under the same irradiation conditions. These results confirmed that **P2-CBA** exhibits favorable tumor accumulation and photothermal effects *in vivo*.

3.9. In vivo antitumor efficacy

Finally, we investigated the *in vivo* synergistic therapeutic effect of **P2-CBA@DOX** on tumor-bearing BALB/c nude mice (Fig. 7a). As shown in Fig. 7b, the treatment groups exhibited varying degrees of tumor growth inhibition when compared with the PBS group. Without laser irradiation, the **P2@DOX** and **P2-CBA@DOX** groups exhibited slower rates of tumor growth inhibition, similar to that of the free DOX group. This reflected the inadequacy of DOX alone in tumor inhibition. In the phototherapy groups, a significant tumor growth suppression effect was observed. Notably, near-complete tumor elimination was achieved in the **P2-CBA@DOX + Laser** group by day 18 after three rounds of treatment. Meanwhile, the **P2-CBA + Laser** group also showed a significant inhibition effect. However, tumor growth reappeared in the **P2@CBA + Laser** group (no DOX) by day 24, whereas no recurrence was observed in the **P2-CBA@DOX + Laser** group throughout the observation period. The photographs and average weights of the tumors after 30 days of treatment are shown in Fig. 7c and **d,** respectively. These findings further demonstrated the excellent tumor ablation in the **P2-CBA@DOX + Laser** group. Additionally, the body weight of the mice did not change significantly in any of the groups within the 30-day experimental period (Fig. 7e), suggesting that these treatments did not induce significant adverse effects on the animals.

Finally, H&E and immunohistochemistry (IHC) staining of tumor tissues were conducted to assess the antitumor effects after 30 days of treatment to evaluate antitumor effects. As shown in Fig. 7f–H&E staining results exhibited detectable necrosis in the tumor tissues of the treatment groups compared to the PBS control group. Moreover, IHC results revealed that these groups displayed reduced Ki67 and CD-31 positive cells, along with increased Caspase-3 positive cells (Fig. 7f). Notably, the **P2-CBA + Laser** group demonstrated the significantly

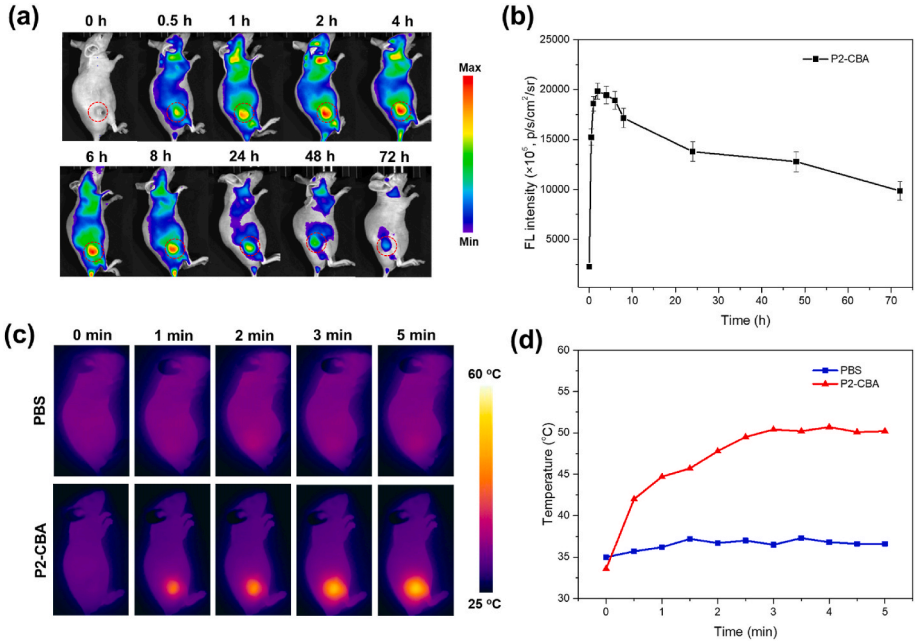

Fig. 6. (a) *In vivo* NIR fluorescence imaging and (b) corresponding fluorescence intensity of tumor-bearing mice after the intravenous injection of P2@CBA. (c) Infrared thermal images and (d) corresponding temperature change curves of tumor-bearing mice after the intravenous injection of PBS and P2-CBA and subsequent 808 nm NIR laser irradiation.

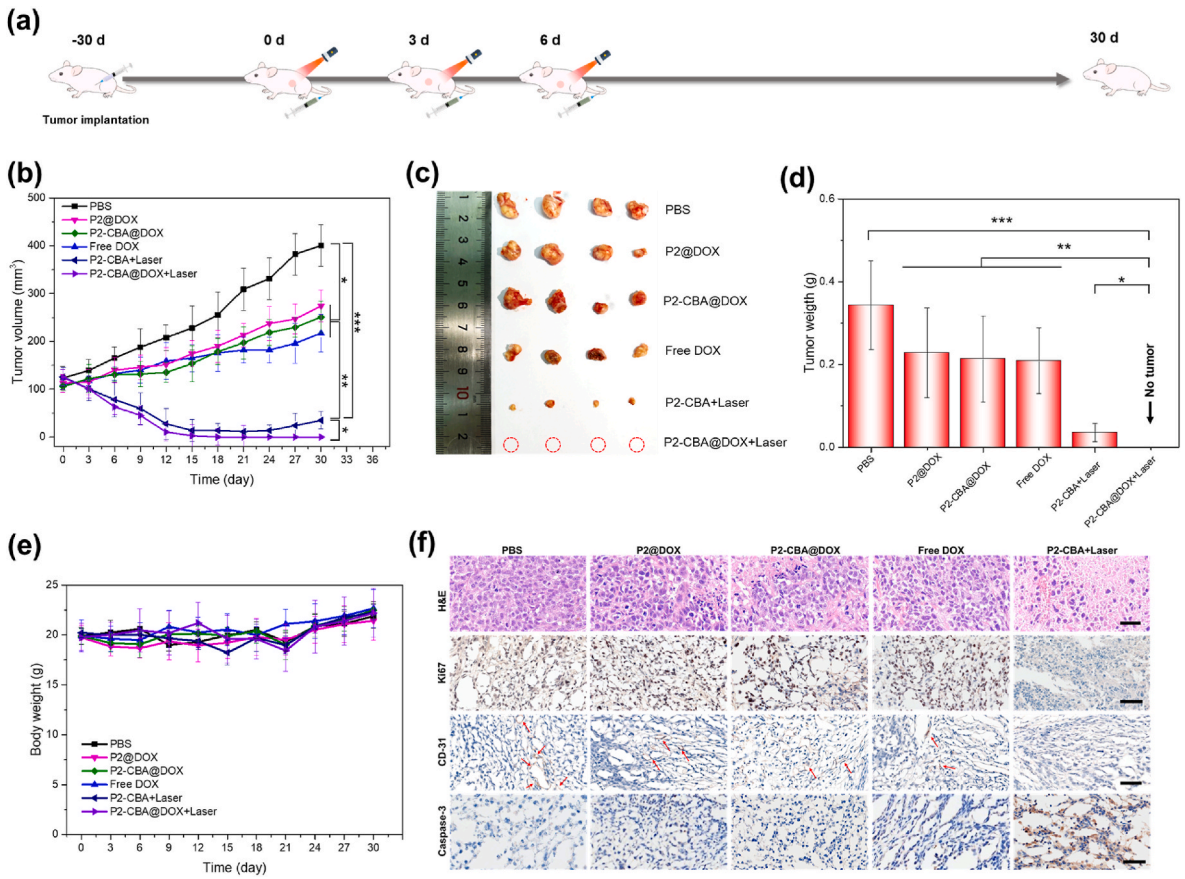

Fig. 7. (a) *In vivo* antitumor treatment procedure. (b) Tumor growth curves of tumor-bearing nude mice in the different treatment groups. (c) Images of tumor anatomy and (d) the average weight of excised tumors at 30 days post-treatment. (e) Body weight changes in the mice during the study periods. (f) H&E and immunohistochemistry staining of tumor tissues at 30 days post-treatment across different treatment groups. Scale bar = 50 μm. Data are expressed as the mean ± SD (n = 4, $*p < 0.05$; $**p < 0.01$; $***p < 0.001$).

enhanced efficacy than DOX-containing groups in both H&E and IHC experiments. These findings suggest that both DOX release and NIR laser irradiation contributed to the tumor inhibition. In fact, the **P2-CBA@-DOX + Laser** group exhibited the most substantial tumor suppression, showing complete necrosis of the tumor at 30 days post-treatment. These data suggested that the disappearance of tumor tissue in this group results from the combined effects of photothermal and chemotherapy, with phototherapy serving as the primary mode and chemotherapy providing additional support. Additionally, H&E staining was conducted to evaluate systemic toxicity in major organs (Fig. S21), confirming the minimal adverse effects of the treatment on healthy tissues. These results further demonstrated that **P-CBA@DOX** exhibited minimal systematic toxicity against normal organs while eliminating tumors via synergistic therapeutic effects.

It is conceivable that complete tumor suppression can be achieved with chemotherapy alone by increasing the dosage of the chemotherapeutic agent. However, this approach causes significant adverse effects. In contrast, the effects of phototherapy alone are hindered by the influence of tumor size and the rapid attenuation of laser intensity in deeper tumor tissues. In this context, the dual-modal antitumor system developed in this study — which primarily relies on physical thermal injury and enables continuous DOX release within tissues — may yield optimal clinical outcomes in the future by addressing these limitations.

4. Conclusion

In this study, we developed a novel class of bi-functional polymeric carriers formed by the co-assembly of GSH-responsive LC-BCPs with a croconaine-based photothermal amphiphile (**CBA**). The disulfide bonds in the pendant groups of the LC blocks could modulate the LC ordering effect and reduction responsiveness of the LC-BCPs. A moderate content of disulfide bonds enabled the micelles formed by **P2** to exhibit relatively higher encapsulation efficiencies for DOX along with improved stability and a suitable reduction-responsiveness. Notably, instead of simple encapsulation, the **CBA** designed in this study could undergo co-assembly with the LC-BCPs and become integrated into the micellar carrier (50 % co-assembly rate) due to the shared cholesterol moiety between the BCPs and the amphiphile. By adjusting the weight ratio of **P2** to **CBA** to 1:2, vesicular co-micelles could be obtained, facilitating the flexible and effective encapsulation of various drugs. Furthermore, both **P2** and **CBA** were found to exhibit excellent biocompatibility, with **CBA** maintaining significant cell viability (>80 %) even at higher concentrations of 200 μg/mL. *In vitro* studies of **P2**-based micelles demonstrated appropriate levels of drug release triggered by the presence of GSH within tumor cells, indicating the high stability of the co-micelles, which could be attributed to their intrinsic LC arrangement. Under NIR laser irradiation, effective cell death was observed via the photothermal effects of the co-micelles and the accelerated reduction-responsive release of DOX. The observed apoptosis following laser irradiation aligns with previous literature indicating that heat-induced cellular stress can activate apoptosis-related pathways, particularly the intrinsic mitochondrial pathway. Additionally, heat shock increases levels of reactive oxygen species (ROS), autophagy, and apoptosis [66]. These findings suggest that the combined treatment not only enhances cell death but also modulates the cell death mechanism toward apoptosis rather than necrosis, a shift that may offer therapeutic benefits such as reduced inflammatory responses and improved safety. *In vivo* experiments further revealed that these co-micelles possessed desirable NIR

fluorescence imaging, tumor accumulation, and retention properties, leading to enhanced synergistic photothermal-chemotherapeutic outcomes. This combination treatment approach, which is primarily based on photothermal therapy supplemented by chemotherapy, is expected to improve therapeutic efficacy while mitigating the long-standing adverse effects associated with chemotherapy. In this study, we primarily investigated the preparation and properties of bifunctional nanoplatforms for synergistic therapy. Regrettably, active targeted therapy has been less explored, but our findings reveal that these co-micelles can be modified in-situ in a straightforward and effective manner. To further enhance the potential for personalized treatment and optimized therapeutic outcomes while minimizing side effects, our future research will prioritize identifying specific targeting groups rather than commonly used ones, and incorporating targeted anti-cancer agents to expand the repertoire of options available for clinical antitumor therapy.

CRediT authorship contribution statement

Yue Lu: Writing – original draft, Investigation, Data curation. **Tiantian Cai:** Formal analysis. **Juanjuan Gao:** Data curation. **Yangge Ren:** Investigation. **Yi Ding:** Visualization, Investigation. **Shujing Liu:** Investigation. **Linyuan Liu:** Validation. **Hao Huang:** Validation. **Haijie Wang:** Resources. **Chengji Wang:** Resources. **Wei Wang:** Resources. **Ruling Shen:** Writing – review & editing, Resources. **Bo Zhu:** Writing – review & editing, Resources. **Lin Jia:** Writing – review & editing, Supervision, Conceptualization.

Declaration of Competing Interest

The authors declare that they have no known competing financial interests or personal relationships that could have appeared to influence the work reported in this paper.

Acknowledgments

This work is supported by the National Natural Science Foundation of China (No. 21871176) and the Science and Technology Commission of Shanghai Municipality (No. 22DZ2291200).

Appendix A. Supplementary data

Supplementary data to this article can be found online at https://doi.org/10.1016/j.mtbio.2024.101355.

Data availability

The authors do not have permission to share data.

References

[1] R.L. Siegel, A.N. Giaquinto, A. Jemal, Cancer statistics, CA A Cancer J. Clin. 74 (1) (2024) 12–49, 2024.
[2] Z. Du, Y. Mao, P. Zhang, J. Hu, J. Fu, Q. You, J. Yin, TPGS–galactose-modified polydopamine co-delivery nanoparticles of nitric oxide donor and doxorubicin for targeted chemo–photothermal therapy against drug-resistant hepatocellular carcinoma, ACS Appl. Mater. Interfaces 13 (30) (2021) 35518–35532.
[3] Z. Li, S. Tan, S. Li, Q. Shen, K. Wang, Cancer drug delivery in the nano era: an overview and perspectives, Oncol. Rep. 38 (2) (2017) 611–624.
[4] L. Marchandet, M. Lallier, C. Charrier, M. Baud'huin, B. Ory, F. Lamoureux, Mechanisms of resistance to conventional therapies for osteosarcoma, Cancers 13 (4) (2021).
[5] B. Chao, J. Jiao, L. Yang, Y. Wang, W. Jiang, T. Yu, L. Wang, H. Liu, H. Zhang, Z. Wang, M. Wu, Application of advanced biomaterials in photothermal therapy for malignant bone tumors, Biomater. Res. 27 (1) (2023).
[6] W. Fan, B. Yung, P. Huang, X. Chen, Nanotechnology for multimodal synergistic cancer therapy, Chem. Rev. 117 (22) (2017) 13566–13638.
[7] W. Ma, Y. Gao, Z. Ouyang, Y. Fan, H. Yu, M. Zhan, H. Wang, X. Shi, M. Shen, Apoptosis-enhanced ferroptosis therapy of pancreatic carcinoma through PAMAM dendrimer-iron(III) complex-based plasmid delivery, Sci. China Chem. 65 (4) (2022) 778–788.
[8] D. Meng, S. Yang, Y. Yang, L. Zhang, L. Cui, Synergistic chemotherapy and phototherapy based on red blood cell biomimetic nanomaterials, J. Control. Release 352 (2022) 146–162.
[9] W. Bian, Y. Wang, Z. Pan, N. Chen, X. Li, W.-L. Wong, X. Liu, Y. He, K. Zhang, Y.-J. Lu, Review of functionalized nanomaterials for photothermal therapy of cancers, ACS Appl. Nano Mater. 4 (11) (2021) 11353–11385.
[10] X. Cui, Q. Ruan, X. Zhuo, X. Xia, J. Hu, R. Fu, Y. Li, J. Wang, H. Xu, Photothermal nanomaterials: a powerful light-to-heat converter, Chem. Rev. 123 (11) (2023) 6891–6952.
[11] W.S. Yun, J.-H. Park, D.-K. Lim, C.-H. Ahn, I.-C. Sun, K. Kim, How did conventional nanoparticle-mediated photothermal therapy become "hot" in combination with cancer immunotherapy? Cancers 14 (8) (2022).
[12] L. Gong, L. Yan, R. Zhou, J. Xie, W. Wu, Z. Gu, Two-dimensional transition metal dichalcogenide nanomaterials for combination cancer therapy, J. Mater. Chem. B 5 (10) (2017) 1873–1895.
[13] Y. Song, K.B. Tan, S.-F. Zhou, G. Zhan, Biocompatible copper-based nanocomposites for combined cancer therapy, ACS Biomater. Sci. Eng. 10 (6) (2024) 3673–3692.
[14] Z. Sun, H. Xie, S. Tang, X.F. Yu, Z. Guo, J. Shao, H. Zhang, H. Huang, H. Wang, P. K. Chu, Ultrasmall black phosphorus quantum dots: synthesis and use as photothermal agents, Angew. Chem. Int. Ed. 54 (39) (2015) 11526–11530.
[15] Z. Yang, X. Yang, Y. Guo, H. Kawasaki, A review on gold nanoclusters for cancer phototherapy, ACS Appl. Bio Mater. 6 (11) (2023) 4504–4517.
[16] A. Setia, R.R. Challa, B. Vallamkonda, P. Satti, A.K. Mehata, V. Priya, S. Kumar, M. S. Muthu, Nanomedicine and nanotheranostics: special focus on imaging of anticancer drugs induced cardiac toxicity, Nanotheranostics 8 (4) (2024) 473–496.
[17] R. Wang, Y. Han, B. Sun, Z. Zhao, Y. Opoku-Damoah, H. Cheng, H. Zhang, J. Zhou, Y. Ding, Deep tumor penetrating bioparticulates inspired burst intracellular drug release for precision chemo-phototherapy, Small 14 (12) (2018).
[18] G. Martínez-Edo, E.Y. Xue, S.Y.Y. Ha, I. Pontón, J.A. González-Delgado, S. Borrós, T. Torres, D.K.P. Ng, D. Sánchez-García, Nanoparticles for triple drug release for combined chemo- and photodynamic therapy, Chem. Eur J. 27 (59) (2021) 14610–14618.
[19] Z. Zhang, W. Tang, Y. Li, Y. Cao, Y. Shang, Bioinspired conjugated tri-porphyrin-based intracellular pH-sensitive metallo-supramolecular nanoparticles for near-infrared photoacoustic imaging-guided chemo- and photothermal combined therapy, ACS Biomater. Sci. Eng. 7 (9) (2021) 4503–4508.
[20] L. Tang, F. Zhang, F. Yu, W. Sun, M. Song, X. Chen, X. Zhang, X. Sun, Croconaine nanoparticles with enhanced tumor accumulation for multimodality cancer theranostics, Biomaterials 129 (2017) 28–36.
[21] Y. Chen, L. Li, W. Chen, H. Chen, J. Yin, Near-infrared small molecular fluorescent dyes for photothermal therapy, Chin. Chem. Lett. 30 (7) (2019) 1353–1360.
[22] R.C.H. Wong, D.K.P. Ng, W.P. Fong, P.C. Lo, Encapsulating pH-responsive doxorubicin–phthalocyanine conjugates in mesoporous silica nanoparticles for combined photodynamic therapy and controlled chemotherapy, Chem. Eur J. 23 (65) (2017) 16505–16515.
[23] K.M. Aijun Zhu, Yibin Deng, Hengte Ke, Hui He, TaoYang, Miao Guo, Yanli Li, Zhengqing Guo, Yangyun Wang, Xiangliang Yang, Youliang Zhao, Huabing Chen, Dually pH/reduction-responsive vesicles for ultrahigh-contrast fluorescence imaging and thermochemotherapy-synergized tumor ablation, ACS Nano 9 (8) (2015) 7874–7885.
[24] D. Wu, Z. Xu, Z. Li, W. Yuan, H.-Q. Wang, X. Xie, Reduction and temperature dually-triggered size-shrinkage and drug release of micelles for synergistic photothermal-chemotherapy of cancer, Eur. Polym. J. 154 (2021).
[25] X. Li, M. Bottini, L. Zhang, S. Zhang, J. Chen, T. Zhang, L. Liu, N. Rosato, X. Ma, X. Shi, Y. Wu, W. Guo, X.-J. Liang, Core–satellite nanomedicines for in vivo real-time monitoring of enzyme-activatable drug release by fluorescence and photoacoustic dual-modal imaging, ACS Nano 13 (1) (2018) 176–186.
[26] W. Yang, X. Shi, Y. Shi, D. Yao, S. Chen, X. Zhou, B. Zhang, Beyond the roles in biomimetic chemistry: an insight into the intrinsic catalytic activity of an enzyme for tumor-selective phototheranostics, ACS Nano 12 (12) (2018) 12169–12180.
[27] X. An, A. Zhu, H. Luo, H. Ke, H. Chen, Y. Zhao, Rational design of multi-stimuli-responsive nanoparticles for precise cancer therapy, ACS Nano 10 (6) (2016) 5947–5958.
[28] X. Chen, F. Li, R. Liang, W. Liu, H. Ma, T. Lan, J. Liao, Y. Yang, J. Yang, N. Liu, A smart benzothiazole-based conjugated polymer nanoplatform with multistimuli response for enhanced synergistic chemo-photothermal cancer therapy, ACS Appl. Mater. Interfaces 15 (13) (2023) 16343–16354.
[29] Z. Guo, S. Zhu, Y. Yong, X. Zhang, X. Dong, J. Du, J. Xie, Q. Wang, Z. Gu, Y. Zhao, Synthesis of BSA-coated BiOI@Bi2S3 semiconductor heterojunction nanoparticles and their applications for radio/photodynamic/photothermal synergistic therapy of tumor, Adv. Mater. 29 (44) (2017) 1704136.
[30] Z. He, W. Chen, K. Hu, Y. Luo, W. Zeng, X. He, T. Li, J. Ouyang, Y. Li, L. Xie, Y. Zhang, Q. Xu, S. Yang, M. Guo, W. Zou, Y. Li, L. Huang, L. Chen, X. Zhang, Q. Saiding, R. Wang, M.-R. Zhang, N. Kong, T. Xie, X. Song, W. Tao, Resolvin D1 delivery to lesional macrophages using antioxidative black phosphorus nanosheets for atherosclerosis treatment, Nat. Nanotechnol. 19 (2024) 1386–1398.
[31] Z. Meng, Y. Liu, K. Xu, X. Sun, Q. Yu, Z. Wu, Z. Zhao, Biomimetic polydopamine-modified silk fibroin/curcumin nanofibrous scaffolds for chemo-photothermal therapy of bone tumor, ACS Omega 6 (34) (2021) 22213–22223.
[32] H. Zhang, Y. Li, Z. Pan, Y. Chen, Z. Fan, H. Tian, S. Zhou, Y. Zhang, J. Shang, B. Jiang, F. Wang, F. Luo, Z. Hou, Multifunctional nanosystem based on graphene oxide for synergistic multistage tumor-targeting and combined chemo-photothermal therapy, Mol. Pharmaceutics 16 (5) (2019) 1982–1998.

[33] Q. Zou, M. Abbas, L. Zhao, S. Li, G. Shen, X. Yan, Biological photothermal nanodots based on self-assembly of peptide–porphyrin conjugates for antitumor therapy, J. Am. Chem. Soc. 139 (5) (2017) 1921–1927.
[34] C. Wang, B. Huang, G. Yang, Y. Ouyang, J. Tian, W. Zhang, NIR-triggered multifunctional and degradable nanoplatform based on an ROS-sensitive block copolymer for imaging-guided chemo-phototherapy, Biomacromolecules 20 (11) (2019) 4218–4229.
[35] Y. Ding, W. Yu, J. Wang, Y. Ma, C. Wang, Y. Wang, B. Lu, Y. Yao, Intelligent supramolecular nanoprodrug based on anionic water-soluble [2]biphenyl-extended-pillar[6]arenes for combination therapy, ACS Macro Lett. 11 (7) (2022) 830–834.
[36] B.-K. Wang, X.-F. Yu, J.-H. Wang, Z.-B. Li, P.-H. Li, H. Wang, L. Song, P.K. Chu, C. Li, Gold-nanorods-siRNA nanoplex for improved photothermal therapy by gene silencing, Biomaterials 78 (2016) 27–39.
[37] X. Song, Q. Chen, Z. Liu, Recent advances in the development of organic photothermal nano-agents, Nano Res. 8 (2) (2014) 340–354.
[38] Q. Feng, Y. Zhang, W. Zhang, Y. Hao, Y. Wang, H. Zhang, L. Hou, Z. Zhang, Programmed near-infrared light-responsive drug delivery system for combined magnetic tumor-targeting magnetic resonance imaging and chemo-phototherapy, Acta Biomater. 49 (2017) 402–413.
[39] H.-J. Yoon, H.-S. Lee, J.-Y. Lim, J.-H. Park, Liposomal indocyanine green for enhanced photothermal therapy, ACS Appl. Mater. Interfaces 9 (7) (2017) 5683–5691.
[40] L. Hosta-Rigau, Y. Zhang, B.M. Teo, A. Postma, B. Städler, Cholesterol – a biological compound as a building block in bionanotechnology, Nanoscale 5 (1) (2013) 89–109.
[41] X. Zhang, L. Han, M. Liu, K. Wang, L. Tao, Q. Wan, Y. Wei, Recent progress and advances in redox-responsive polymers as controlled delivery nanoplatforms, Mater. Chem. Front. 1 (5) (2017) 807–822.
[42] P. Kumar, S.-H. Kim, S. Yadav, S.-H. Jo, S. Yoo, S.-H. Park, K.T. Lim, Redox-responsive core-cross-linked micelles of miktoarm poly(ethylene oxide)-*b*-poly (furfuryl methacrylate) for anticancer drug delivery, ACS Appl. Mater. Interfaces 15 (10) (2023) 12719–12734.
[43] F. Meng, W.E. Hennink, Z. Zhong, Reduction-sensitive polymers and bioconjugates for biomedical applications, Biomaterials 30 (12) (2009) 2180–2198.
[44] Y. Lu, Y. Ren, J. Gao, T. Cai, L. Liu, Y. Ding, Q. Xie, L. Jia, Fabrication of hierarchical nanostructures featuring amplified asymmetry through Co-assembly of liquid crystalline block copolymer and chiral amphiphiles, Angew. Chem., Int. Ed. (2024) e202417573.
[45] X. Song, J.W. Foley, A new water-soluble near-infrared croconium dye, Dyes Pigments 78 (1) (2008) 60–64.
[46] Y. Lu, J. Gao, Y. Ren, Y. Ding, L. Jia, Synergetic self-assembly of liquid crystalline block copolymer with amphiphiles for fabrication of hierarchical assemblies, Small 20 (1) (2023).
[47] L.J. Rafael Piñ ol, Francesca Gubellini, Daniel Lévy, Pierre-Antoine Albouy, Patrick Keller, Amin Cao, Min-Hui Li, Self-assembly of PEG-*b*-liquid crystal polymer: the role of smectic order in the formation of nanofibers, Macromolecules 40 (16) (2007) 5625–5627.
[48] L. Jia, A. Cao, D. Lévy, B. Xu, P.-A. Albouy, X. Xing, M.J. Bowick, M.-H. Li, Smectic polymer vesicles, Soft Matter 5 (18) (2009).
[49] L. Li, F. Zhou, Y. Li, X. Chen, Z. Zhang, N. Zhou, X. Zhu, Cooperation of amphiphilicity and smectic order in regulating the self-assembly of cholesterol-functionalized brush-like block copolymers, Langmuir 34 (37) (2018) 11034–11041.
[50] L. Jia, P.-A. Albouy, A. Di Cicco, A. Cao, M.-H. Li, Self-assembly of amphiphilic liquid crystal block copolymers containing a cholesteryl mesogen: effects of block ratio and solvent, Polymer 52 (12) (2011) 2565–2575.
[51] J. Tan, Z. Deng, G. Liu, J. Hu, S. Liu, Anti-inflammatory polymersomes of redox-responsive polyprodrug amphiphiles with inflammation-triggered indomethacin release characteristics, Biomaterials 178 (2018) 608–619.
[52] Z. Cao, X. Zhou, G. Wang, Selective release of hydrophobic and hydrophilic cargos from multi-stimuli-responsive nanogels, ACS Appl. Mater. Interfaces 8 (42) (2016) 28888–28896.
[53] Z. Cao, H. Wu, J. Dong, G. Wang, Quadruple-stimuli-sensitive polymeric nanocarriers for controlled release under combined stimulation, Macromolecules 47 (24) (2014) 8777–8783.
[54] E.D. Sultanova, A.A. Atlanderova, R.D. Mukhitova, V.V. Salnikov, Y.N. Osin, A. Y. Ziganshina, A.I. Konovalov, Reduction-controlled substrate release from a polymer nanosphere based on a viologen-cavitand, RSC Adv. 6 (74) (2016) 70072–70076.
[55] F. Chen, L. Yin, T. He, T. Chen, H. Yue, C. Yang, Fabrication of dual pH/reduction-responsive P(CL-co-ACL)-based cross-linked polymeric micelles for PTX delivery, Langmuir 39 (46) (2023) 16358–16366.
[56] D. Biswas, S.Y. An, Y. Li, X. Wang, J.K. Oh, Intracellular delivery of colloidally stable core-cross-linked triblock copolymer micelles with glutathione-responsive enhanced drug release for cancer therapy, Mol. Pharmaceutics 14 (8) (2017) 2518–2528.
[57] L. Jia, D. Cui, J. Bignon, A. Di Cicco, J. Wdzieczak-Bakala, J. Liu, M.-H. Li, Reduction-responsive cholesterol-based block copolymer vesicles for drug delivery, Biomacromolecules 15 (6) (2014) 2206–2217.
[58] H.S. Jung, P. Verwilst, A. Sharma, J. Shin, J.L. Sessler, J.S. Kim, Organic molecule-based photothermal agents: an expanding photothermal therapy universe, Chem. Soc. Rev. 47 (7) (2018) 2280–2297.
[59] L. Liu, M.-H. Liu, L.-L. Deng, B.-P. Lin, H. Yang, Near-infrared chromophore functionalized soft actuator with ultrafast photoresponsive speed and superior mechanical property, J. Am. Chem. Soc. 139 (33) (2017) 11333–11336.
[60] Y. Yin, L. Gao, P. Sun, L. Zeng, Q. Zhao, S. Chen, J. Liu, L. Wang, pH/ROS dual stimuli-responsive anionic flexible supramolecular organic frameworks for synergistic therapy, Acta Biomater. 172 (2023) 395–406.
[61] A. Blanazs, S.P. Armes, A.J. Ryan, Self-Assembled block copolymer aggregates: from micelles to vesicles and their biological applications, Macromol. Rapid Commun. 30 (4–5) (2009) 267–277.
[62] L. Rulíšek, P. Šebek, Z. Havlas, R. Hrabal, P. Čapek, A. Svatos, An experimental and theoretical study of stereoselectivity of furan-maleic anhydride and furan-maleimide diels-alder reactions, J. Org. Chem. 70 (2005) 6295–6302.
[63] M. Vauthier, L. Jierry, M.L. Martinez Mendez, Y.-M. Durst, J. Kelber, V. Roucoules, F. Bally-Le Gall, Interfacial diels–alder reaction between furan-functionalized polymer coatings and maleimide-terminated poly(ethylene glycol), J. Phys. Chem. C 123 (7) (2019) 4125–4132.
[64] D. Kasala, S.-H. Lee, J.W. Hong, J.-W. Choi, K. Nam, Y.H. Chung, S.W. Kim, C.-O. Yun, Synergistic antitumor effect mediated by a paclitaxel-conjugated polymeric micelle-coated oncolytic adenovirus, Biomaterials 145 (2017) 207–222.
[65] F. Yu, F. Zhang, L. Tang, J. Ma, D. Ling, X. Chen, X. Sun, Redox-responsive dual chemophotothermal therapeutic nanomedicine for imaging-guided combinational therapy, J. Mater. Chem. B 6 (33) (2018) 5362–5367.
[66] S. Kassis, M. Grondin, D.A. Averill-Bates, Heat shock increases levels of reactive oxygen species, autophagy and apoptosis, BBA - Molecular Cell Research 1868 (3) (2021).